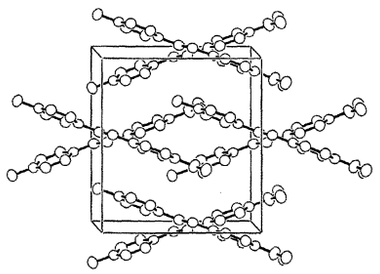

Fig. 3. Packing diagram for the same compound viewed approximately along the *c* axis (tosylate anions have been removed for clarity).

cent rows of cationic chromophores in a parallel manner (Figs. 2 and 3). The perpendicular distance between chromophores within a stack is about 3.4 Å, suggesting that the excellent alignment of the chromophores within a given row may be assisted by π-stacking. The only deviation from a completely aligned system is the 20° angle between the long axis of the molecules and the polar *a* axis of the crystal. In space group *Cc* the optimal angle for phase matching (*20*) is 35.3° between the charge-transfer axis of the nonlinear chromophore and the *b* axis of the crystal and, as such, the observed orientation is not well optimized for SHG, yet the powder efficiencies are large. In any case, given this excellent alignment in the crystal, extremely large electro-optic coefficients are expected (if the β_{zzz} is along the charge-transfer axis, then 83% of β_{zzz} is maintained along the polar *a* axis).

Our results demonstrate that the organic "salt methodology" can be used to obtain materials with very large $\chi^{(2)}$. Further, it has been shown that nonconventional donors such as Br^- and the pyrenyl moiety can be incorporated into molecules that, in the correct crystallographic environment, exhibit substantial bulk susceptibilities. We believe that this study represents an important step in decoupling the design of desirable molecular properties (large molecular nonlinearity and transparency) from the dipolar orientational requirements of $\chi^{(2)}$ materials. If the counterion is covalently linked to the ionic chromophore, then many of the desirable features of the "salt methodology" (large β and large dipole moment) can be used productively in an oriented polymer format.

REFERENCES AND NOTES

1. D. J. Williams, *Angew. Chem. Int. Ed. Engl.* **23**, 690 (1984).
2. D. J. Williams, Ed., *Nonlinear Optical Properties of Organic and Polymeric Materials* (ACS Symposium Series 233, American Chemical Society, Washington, DC, 1983).
3. D. S. Chemla and J. S. Zyss, Eds., *Nonlinear Optical Properties of Organic Molecules and Crystals* (Academic Press, Orlando, FL, 1987).
4. J. L. Oudar and D. S. Chemla, *J. Chem. Phys.* **66**, 2664 (1977); B. F. Levine and C. G. Bethea, *ibid.*, p. 1070; S. J. Lalama and A. F. Garito, *Phys. Rev. A* **20**, 1179 (1979).
5. J. F. Nicoud and R. W. Twieg, in (*3*), vol. 1, p. 242.
6. R. W. Twieg and K. Jain, in (*2*), p. 57.
7. J. S. Zyss, J. F. Nicoud, M. Koquillay, *J. Chem. Phys.* **81**, 4160 (1984).
8. J. S. Zyss *et al.*, *ibid.* **74**, 4800 (1981).
9. S. Tomaru *et al.*, *J. Chem. Soc. Chem. Commun.* **1984**, 1207 (1984); W. Tam *et al.*, *Chem. Mater.* **1**, 128 (1989); I. Weissbuch *et al.*, *ibid.*, p. 114.
10. S. D. Cox, T. E. Gier, J. D. Bierlein, G. D. Stucky, *J. Am. Chem. Soc.* **110**, 2986 (1989).
11. K. D. Singer, J. E. Sohn, S. J. Lalama, *Appl. Phys. Lett.* **49**, 248 (1986).
12. G. R. Meredith, in (*2*), p. 30.
13. W. Tam, Y. Wang, J. C. Calabrese, R. A. Clement, *Proc. Soc. Photo.-Opt. Instrum. Eng.* **971**, 107 (1988).
14. M. L. H. Green *et al.*, *Nature* **330**, 360 (1987).
15. S. R. Marder and J. W. Perry, in preparation.
16. Synthetic details will be described elsewhere: S. R. Marder *et al.*, in preparation.
17. S. K. Kurtz and T. T. Perry, *J. Appl. Phys.* **39**, 3798 (1968).
18. The Cl^- salts are hygroscopic, which is evidenced by elemental analysis, differential scanning calorimetry, and thermogravimetric analysis. We have not obtained satisfactory analysis for the Cl^- salts, although the agreement improves when calculated as some form of hydrate. Despite this, we can obtain reproducible SHG efficiencies, which are dependent on the degree of hydration.
19. $C_{23}H_{26}N_2SO_3$; molecular weight, 410.54; monoclinic, *Cc*(#9), a = 10.365(3) Å, b = 11.322(4) Å, c = 17.893(4) Å, β = 92.24(2)°, V = 2098.2(11) Å^3, Z = 4, where β is the crystallographic angle between a and c, V is the cell volume, and Z is the number of formula units per cell (figures in parentheses are the estimated standard deviations in the last figure). MoKα radiation, 3891 reflections collected, 1850 independent reflections used in full matrix least-squares refinement, for 1777 reflections with $F_o^2 > 0$; R ($\Sigma \mid F_o - \mid F_c \mid\mid / \Sigma F_o$, where F is the structure factor) = 0.033, goodness of fit $([\Sigma w(F_o^2 - F_c^2)^2/(n - p)]^{1/2}$, where w is the weight of the reflection, n is the number of data, p is the number of parameters refined) = 1.81, and subscripts o and c refer to observed and calculated values, respectively. All nonhydrogens refined anisotropically. Hydrogen atom parameters were assigned from difference maps or by calculation with C–H = 0.95 Å.
20. J. S. Zyss and J. L. Oudar, *Phys. Rev. A* **26**, 2028 (1982).

21. This research was performed at the Jet Propulsion Laboratory (JPL), California Institute of Technology, as part of its Innovative Space Technology Center, which is supported by the Strategic Defense Initiative Organization through an agreement with the National Aeronautics and Space Administration (NASA). S.R.M. was supported by a NASA National Research Council Resident Research Associateship at JPL, and he thanks R. Grubbs for access to synthetic facilities. The diffractometer used in this study was purchased with a grant from the National Science Foundation. We thank B. G. Tiemann, P. Groves, and K. J. Perry for technical assistance.

3 April 1989; accepted 6 June 1989

Scandinavian, Siberian, and Arctic Ocean Glaciation: Effect of Holocene Atmospheric CO_2 Variations

D. R. LINDSTROM AND D. R. MACAYEAL

A computer model of coupled ice sheet–ice shelf behavior was used to evaluate whether observed changes in atmospheric CO_2 concentration could have caused the advance and retreat of Pleistocene ice sheets in the Eurasian Arctic. For CO_2 concentrations below a threshold of approximately 250 parts per million, an extensive marine-based ice sheet covering Scandinavia, the Barents, Kara, and East Siberian seas, and parts of the Arctic Ocean developed in the model simulations. In the simulations, climatic warming associated with the Holocene rise of atmospheric CO_2 was sufficient to collapse this widespread glaciation and restore present-day ice conditions.

ICE CORE RECORDS SUGGEST THAT Pleistocene glacial episodes are associated with significant depletion of CO_2 in the atmosphere (*1*). The effect of this depletion on atmospheric temperature and water transport may account for the intensity and global synchronization of the glacial response to orbital variations (*2, 3*). In an effort to test this hypothesis, we conducted computer simulations of ice-sheet behavior in the Eurasian Arctic under specific climatic conditions (*4*). We focused our study on the Eurasian Arctic because the grounding of ice on its broad continental shelves and the development of thick floating ice shelves offshore may have reorganized Arctic Ocean thermohaline circulation (*5*). Under present conditions, sea-ice formation in the shallow seas of the Eurasian Arctic produces brine-enriched waters that drain into the deep and intermediate levels of the Arctic Ocean. Grounded ice-sheet expansion across these seas under glacial conditions would thus alter the thermohaline circulation and density stratification of the Arctic Ocean and the Norwegian and Greenland seas. These oceanographic consequences of Eurasian glaciation could account for decreased North Atlantic deep water production rates during the last glacial maximum (LGM) (*6*).

Our model predicts the two-dimensional horizontal flow, mass balance, and three-dimensional temperature distribution of an ice sheet in response to specified atmospheric boundary conditions (surface accumula-

D. R. Lindstrom, Department of Geological Sciences (M/C 186), College of Liberal Arts and Sciences, University of Illinois at Chicago, Box 4348, Chicago, IL 60680. D. R. MacAyeal, Department of Geophysical Sciences, University of Chicago, Chicago, IL 60637.

tion or ablation rate and surface temperature). The primary difference between our model and those used in earlier studies of Antarctic or Laurentide glaciation (*7*) is rigorous treatment of floating ice shelves that extend into the Arctic Ocean (*8*). This treatment is essential because ice shelves may have played a significant role in both the growth and rapid collapse of marine-based ice sheets in the Barents and Kara seas (*9, 10*). Ice thickness is predicted as a function of time by solution of the mass continuity equation subject to atmospheric forcing described below and specified boundary conditions at the edges of the ice sheet (*11*). Ice velocity is predicted as a function of the instantaneous ice thickness distribution by the use of the time-independent stress-equilibrium equations (*12*) for a non-Newtonian ice rheology that depends on ice temperature and deformation rate (*13*). Temperature of the ice and underlying bedrock is calculated with a vertical conduction-advection equation in order to determine the temperature-dependent rheological parameters, the locations where the bed may have melted, and the subglacial permafrost depth (if the bed is frozen). Crustal motion induced by the changing ice and sea-water surface load is assumed to vary in proportion to the isostatic disequilibrium with a time scale of 5000 years (*14*).

In the ice-sheet model, ice-sheet growth and decay is a function of three atmospheric variables: surface accumulation rate, A (in meters of ice per year per square meter), annual average surface temperature, T (°C), and summer average surface temperature, T_s (°C). By running the model until equilibrium ice-sheet conditions are achieved, we can determine whether a given distribution of these variables is sufficient to support glaciation. Our task is thus to estimate the distributions of T, T_s, and A that result from natural CO_2 variations and from variations in ice-sheet coverage and topography. We expanded T and T_s in a Taylor series about the observed, present-day distributions (T^* and T_s^*) using CO_2 sensitivities derived from general circulation model (GCM) experiments of the atmosphere and ocean, and temperature lapse rates for the standard atmosphere (*15*):

$$T(c, z_s, \phi, \lambda) = T^*(\phi, \lambda) + \Delta c(\partial T/\partial c) + \Delta z_s(\partial T/\partial z_s) \quad (1)$$

$$T_s(c, z_s, \phi, \lambda) = T_s^*(\phi, \lambda) + \Delta c(\partial T/\partial c) + \Delta z_s(\partial T/\partial z_s) \quad (2)$$

where $c(t)$ is the atmospheric CO_2 concentration in parts per million, $z_s(t, \phi, \lambda)$ is the surface elevation of the ice, land, or sea surface, t is time, ϕ is latitude, λ is longitude, $\Delta c = [c(t) - 295]$, $\Delta z_s = [z_s(t) - z_s^*]$, and z_s^* is the observed present-day value of z_s. For the ice accumulation rate, precipitation changes due to CO_2 concentration and ice-sheet surface elevation are too large to allow use of a Taylor-series expansion about present-day distribution of net, annual average precipitation (*16, 17*). We thus assumed that A is proportional to its present, observed distribution, A^*, with the factor of proportionality depending on CO_2 concentration:

$$A(c, z_s, \phi, \lambda) = (1 - \alpha\Delta c)A^*(\phi, \lambda) + \Delta z_s(\partial A/\partial z_s) - M \quad (3)$$

where α is the CO_2 sensitivity coefficient, which is assumed to be a function of latitude, and the ice ablation rate M (in meters per year per square meter) is (*18*)

$$M = \begin{cases} 0.028(12 + T)^2 & \text{if } T_s > 0°C \\ 0 & \text{if } T_s < 0°C \end{cases} \quad (4)$$

To avoid circumstances where ice dome summits would become so high that A becomes negative, we imposed a lower bound of 0.005 m per year wherever $T_s <$ 0°C. Values of Δc used in our simulations of the LGM and the Holocene were taken from the Vostok ice core record. Variation of Δz_s is predicted directly by the model.

The CO_2 sensitivities that we used in our simulations for temperature and ice accumulation (Table 1) were derived from several atmospheric general circulation model (GCM) simulations designed to evaluate the effects of reduced CO_2 on climate (*19*). Our reliance on GCM results may seem to introduce a pivotal uncertainty. Inasmuch as our model determines a relation between model-input variables and simulated ice-sheet size, our simulations provide an independent estimate of climatic conditions necessary to support extensive glaciation. The estimated temperature and accumulation rate sensitivities necessary to support glaciation (Table 1) fall well within the range of sensitivities predicted by the GCM studies (*20*). An additional check on our estimate of temperature sensitivity to CO_2 concentration is provided by the Vostok ice core deuterium record, which suggests that the reductions in temperature at the Vostok site during the LGM (about 9°C) were comparable to those required for ice-sheet growth in our model (*21*).

The sensitivities of temperature and accumulation to ice-sheet surface elevation ($\partial T/\partial z_s$, $\partial T_s/\partial z_s$, and $\partial A/\partial z_s$) were determined from present-day observations and were assumed not to change as a result of changes in atmospheric CO_2 concentration. The lapse rate for surface temperatures ($\partial T/\partial z_s$ and $\partial T/\partial z_s$) was 6.5°C km^{-1}, the tropospheric lapse rate for the U.S. standard atmosphere. This lapse rate is the lower limit of that expected and thus tends to bias forcing in our model toward conditions less favorable to the initiation or maintenance of ice sheets (*22*). A value for $\partial A/\partial z_s$ was derived from a regression analysis of data for ice-sheet accumulation and surface elevation from Antarctica and is -2.5×10^{-5} per year (*23*).

To evaluate whether CO_2-induced climate changes could have produced the LGM ice-sheet configuration and then restored nearly ice-free interglacial conditions, we ran two numerical experiments. In the first experiment, we fixed model input variables (temperatures and ice accumulation rates) at values associated with the LGM CO_2 concentration until an equilibrium ice distribution was achieved (Fig. 1). The model was integrated through 30,000 years from an arbitrary, ice-free initial condition to achieve this equilibrium. In the second experiment, we allowed model input temperatures and ice accumulation to vary according to the CO_2 concentration time series (Fig. 2) derived from the Vostok ice core record. The initial condition was the equilibrium ice configuration derived from the simulation of LGM conditions. Model integration then

Table 1. Mean annual surface temperature changes and accumulation rate amplification factors associated with the 195-ppm atmospheric CO_2 concentration of the LGM (Δc = 100 ppm) (*19*). Also shown are minimum changes required by our model to support extensive glaciation (equivalent to Δc = 50 ppm). Changes in T_s were assumed to be the same as in T.

Latitude (°N)	Changes induced by LGM CO_2 concentrations		Minimum changes needed to support glaciation	
	$\Delta c(\partial T/\partial c)$ (°C)	$(1 - \alpha\Delta c)$	$\Delta c(\partial T/\partial c)$ (°C)	$(1 - \alpha\Delta c)$
90	−18	0.89	−8	0.95
85	−18	0.89	−8	0.95
80	−17	0.31	−8	0.69
75	−17	0.78	−8	0.90
70	−13	0.91	−6	0.96
65	−9	0.93	−4	0.97
60	−9	1.13	−4	1.07
55	−8	1.03	−4	1.02

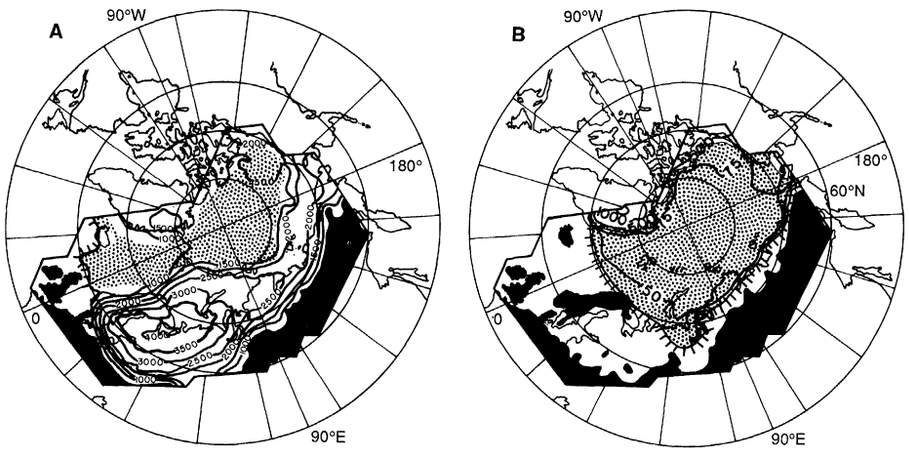

Fig. 1. Simulated ice thickness fields for the equilibrium ice sheet at (**A**) the LGM (c = 195 ppm) and (**B**) collapsed ice sheet after 10,000 years of rise in CO_2 concentrations (8000 years ago). The region of the model grid is enclosed by the polygon. Contours represent ice thickness (in meters), dotted pattern identifies ice shelf (floating ice), and hatched lines indicate the iceberg calving front. Subaerial regions in the model domain not covered by ice are solid black. Ice-free areas in the model grid and areas below sea level in (B) are white, and include continental regions affected by isostatic depression.

proceeded for 18,000 years to determine whether the current interglacial ice configuration could be established. As shown in Fig. 2, the simulated ice sheets began to collapse after approximately 4,000 years (14,000 years ago), and the collapse was completed by 9,000 years (9,000 years ago). At the end of the 18,000-year model integration, the stimulated ice distribution resembled the present-day distributions of Greenland ice and thin Arctic Ocean sea ice (Fig. 1).

The simulated LGM ice-sheet distribution is similar to that reconstructed from geological evidence. Grounded ice covers the Scandinavian region as well as the shallow continental shelves of the European and Siberian Arctic. Various independent evidence suggests that there was a marine-based ice sheet in the Barents and Kara seas (*24*). For the Laptev and East Siberian seas, the LGM distribution produced by our model compares well with reconstructions based on sediment features observed near Novosibirski Ostrova (*25*). The simulated LGM ice-sheet distribution differs from that reconstructed from geological evidence in two ways. First, the North Sea and Great Britain were ice-free in our simulations. Second, the simulated ice sheet extended too far south across eastern Europe. These discrepancies resulted primarily from our estimate of LGM climate conditions. In particular, we did not account for climatic effects associated with the diversion of the North Atlantic Current from the Arctic during glacial periods (*26*). As a result, the specified temperatures over the North Sea and Great Britain were too warm to allow ice-sheet development in our simulation.

The rapid collapse of the simulated LGM ice distribution with rising CO_2 concentration was initiated when the CO_2 concentration reached 250 ppm at 14,000 years ago (6,000 years after the LGM in Fig. 2). This CO_2 concentration corresponds to the temperature threshold required by our model to support widespread glaciation (Table 1). If the GCM-derived estimate of temperature sensitivity to CO_2 concentration is correct, we believe that the 250-ppm value represents an upper bound for the depression in CO_2 concentration necessary to support glacial maximum ice conditions. The simulated ice-sheet collapse depended strongly on two aspects of ice-sheet physics. First, extensive crustal depression caused by ice loads (Fig. 1) allowed thick portions of the ice sheets to unground and flow rapidly toward ablation areas on the southern ice margin and in the Norwegian and Greenland seas. Second, surface warming associated with falling ice-sheet surface elevations and the atmospheric lapse rate amplified the CO_2 warming effect. The difference of grounded ice volume between our simulations of LGM and present-day conditions is 3.2×10^7 km^3 (Fig. 2), and this corresponds to approximately 74 m of eustatic sea-level change (*27*). If the average oxygen isotope ratio of simulated ice is −35 parts per thousand, our results suggest that the oceanic oxygen isotope ratio increased by 0.86 part per thousand as a result of Eurasian ice alone.

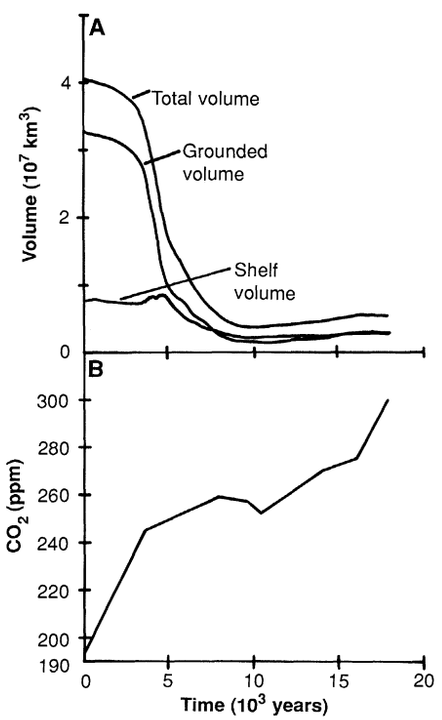

Fig. 2. (**A**) Ice volume curves during simulated Holocene collapse of the Eurasian ice-sheet system. (**B**) The CO_2 concentration curve used to estimate climate conditions specified during ice-sheet collapse.

Our ice-sheet model experiments suggest that natural variations of atmospheric CO_2, as evident in the ice core records, can substantially reorganize the Arctic Ocean and can cause the expansion and retreat of the Eurasian ice sheets. Our results do not rule out other causes of Eurasian ice age glaciation, and our simulated ice-sheet coverage does not display perfect fidelity to geologic reconstructions. It is thus premature to conclude that our model results can be taken as evidence that atmospheric CO_2 variations drove the Pleistocene ice ages. The critical uncertainty which restrains this conclusion is in how atmospheric CO_2 effects surface temperature and snow accumulation on the ice sheets. The GCM studies we examined, however, suggest that climate sensitivity to reduced CO_2 concentration is about twice that needed by our model to support the glacial cycles of the Eurasian Arctic.

REFERENCES AND NOTES

1. J. M. Barnola, D. Raynaud, T. S. Korotkevich, C. Lorius, *Nature* **329**, 408 (1987).
2. J. D. Hays *et al.*, *Science* **194**, 1121 (1976).
3. J. E. Kutzbach and P. J. Guetter, *J. Atmos. Sci.* **43**, 1726 (1986).
4. D. R. Lindstrom, thesis, University of Chicago (1989).
5. K. Aagaard, J. H. Swift, E. C. Carmack, *J. Geophys. Res.* **90**, 4833 (1985).
6. J. C. Duplessy *et al.*, *Paleoceanography* **3**, 343 (1988).
7. See, for example, J. Oerlemans, *Nature* **297**, 550 (1982).
8. The flow dynamics of floating ice differs from that of grounded ice in several important ways. Horizontal deviatoric stresses dominate the stress balance in floating ice shelves because basal friction at the sea water–ice interface is negligible. Horizontal velocity in an ice shelf does not vary with depth. In contrast, the dominant stress balance in grounded ice is between surface slope–induced pressure gradient and basal friction. Horizontal velocity in grounded ice sheets can thus display strong vertical shear, particularly where the ice is frozen to a rigid bed.

9. G. H. Denton and T. J. Hughes, in *The Last Great Ice Sheets*, G. H. Denton and T. J. Hughes, Eds. (Wiley, New York, 1981), pp. 440–467.
10. T. J. Hughes *et al.*, *Nature* **266**, 596 (1977).
11. The mass continuity equation is solved with the finite-element method. Boundary conditions are a mixture of mass flux conditions. At seaward boundaries, horizontal ice flux is passed freely to the model exterior as if balanced by iceberg calving. Land boundaries in Greenland and across North America are set along natural ice divides of the Greenland ice sheet and the past Laurentide ice sheet. Ice flux along these land boundaries is thus set to 0. Basal melting is assumed to be 0 throughout the model domain.
12. The stress-equilibrium equations are solved with the finite-element method. Our treatment of grounded ice is nearly identical to that employed by Oerlemans in a simulation of the Antarctic ice sheet (7). Our treatment of the more spatially complex stress balance in floating ice is identical to that employed previously in studies of Antarctic ice streams and ice shelves [D. R. MacAyeal, *J. Geophys. Res.* **94**, 4071 (1989)].
13. The effective viscosity of ice used in the simulations is based on laboratory ice-deformation tests [P. Barnes, D. Tabor, J. C. F. Walker, *Proc. R. Soc. London Ser. A* **324**, 1557 (1971)].
14. The time constant for isostatic rebound depends on properties of the solid earth and on the horizontal length scale of the applied surface load. The time constant we used was determined with a simple, viscous half-space earth model and an applied load that varied sinusoidally in one horizontal direction with a wavelength of 2000 km.
15. Present-day mean annual and summer temperatures were obtained from H. Walter and H. Lieth [*Klimadigramm Weltatlas* (Fischer Verlag, Jena, German Democratic Republic, 1967)]. Present-day net accumulation rates were obtained from contour plots of present-day precipitation and evaporation rates [V. I. Korzoun, *Atlas of World Water Balance* (Gidrometeoizdat, Leningrad, 1977)].
16. Net ice accumulation rates on the surfaces of present-day ice sheets is comparable to, or less than, the changes in high-latitude precipitation produced by some GCM simulations when CO_2 concentration was reduced from its present value to the value at the LGM. A CO_2-induced change of approximately 0.15 m per year per square meter, for example, was reported by Manabe and Bryan (*17*) for the latitude band encompassing the Eurasian ice sheet.
17. S. Manabe and K. Bryan, *J. Geophys. Res.* **90**, 11689 (1985).
18. J. Oerlemans and C. J. van der Veen, *Ice Sheets and Climate* (Reidel, Hingham, MA, 1984).
19. We derived $\partial T/\partial c$ and $\partial T_s/\partial c$ from ice-free land gridpoints of the VC (variable cloudiness) GCM experiment conducted by Manabe and Broccoli in which CO_2 concentration was 200 ppm and ice-sheet surface topography was specified [S. Manabe and A. J. Broccoli, *J. Atmos. Sci.* **42**, 2643 (1985)]. We derived α from Manabe and Bryan's (*17*) $c = \sqrt{2}X$ coupled atmosphere-ocean model experiment in which CO_2 concentration was 212 ppm. We would prefer to have derived $\partial T/\partial c$, $\partial T_s/\partial c$, and α from a single GCM climate study, but we used two studies because Manabe and Broccoli's study incorporated the effect of ice-sheet topography on atmospheric circulation (which we consider important in determining temperature sensitivity) and Manabe and Bryan's study incorporated oceanic circulation and oceanic temperature and salinity budgets (which we consider important in determining atmospheric water transport). The values of $\Delta c(\partial T/\partial c)$ (under LGM conditions) shown in Table 1 reflect the observation that GCM predictions of cooling reduced CO_2 concentration are amplified at high latitudes. For comparison, the globally averaged difference in surface temperature between LGM and present given by Manabe and Broccoli's VC simulation was −4.7°C. Uncertainty in this global difference evident by other GCM simulations (such as Manabe and Broccoli's FC simulation, which specified fixed cloud distribution) is approximately 1°C.
20. As an additional experiment, we ran the model with $T(\phi, \lambda)$ and $A(\phi, \lambda)$ specified directly from output of Kutzbach and Guetter's (*3*) GCM simulation that incorporated specified LGM sea-surface temperature, reduced atmospheric CO_2 concentration, insolation effects due to orbital geometry, and specified ice-sheet topography. The ice-sheet configuration that resulted agreed well with geological reconstructions. The ice shelf thickness over the Arctic Ocean, however, became unrealistically large.
21. J. Jouzel *et al.*, *Nature* **329**, 403 (1987).
22. The lapse rate over Antarctica, for example, is between 7° and 10°C km^{-1} [J. Oerlemans, in *Dynamics of the West Antarctic Ice Sheet*, C. J. Van der Veen and J. Oerlemans, Eds. (Reidel, Hingham, MA, 1987), pp. 287–292].
23. D. H. Bromwich, *Rev. Geophys.* **26**, 149 (1988).
24. Evidence includes geomorphology of the sea-floor sediments and continental slope debris fans [M. G. Grosswald, *Quat. Res.* **13**, 1 (1980); T. O. Vorren, M. Hald, E. Lebesbye, *Paleoceanography* **3**, 601 (1988)], polar-wander paths and relative sea-level rise [W. R. Peltier, *Science* **240**, 895 (1988)], and deep-sea oxygen-isotope records [G. A. Jones and L. D. Keigwin, *Nature* **336**, 56 (1988)].
25. Evidence includes push-tectonic overthrusts and the distribution of permafrost [M. G. Grosswald, in *Data of Glaciological Studies*, G. A. Avsyok and V. M. Kotlyakov, Eds. (Publ. 63, Academy of Science of the U.S.S.R. Soviet Geography Committee, Moscow, 1988), pp. 3–25.
26. W. F. Ruddiman and A. McIntyre, *Paleogeogr. Paleoclimatol. Paleoecol.* **35**, 145 (1981).
27. The effect of the simulated ice sheet on eustatic sea level may be 30 to 50% higher than previously estimated [G. S. Boulton, G. D. Smith, A. S. Jones, J. Newsome, *J. Geol. Soc. London* **142**, 447 (1985)]. Trial simulations in which we accounted for ice streams that flow across deformable sub-glacial sediment yielded smaller ice-sheet volumes. The total ice volume and its effect on eustatic sea level thus depends strongly on basal boundary conditions associated with the stress equilibrium.
28. We thank A. Anderson, V. Barcilon, T. J. Hughes, C. S. Lingle, M. Monaghan, G. W. Platzman, and A. Ziegler for critical review of the Ph.D. dissertation on which this work is based. J. Kutzbach and R. Selin kindly provided detailed background information concerning their GCM experiments. Model computations were performed on the computers of the National Center for Atmospheric Research. Financial support was provided by National Science Foundation grant DPP 85-09451.

17 April 1989; accepted 21 June 1989

Neural Cadherin: Role in Selective Cell-Cell Adhesion

SEIJI MIYATANI, KENJI SHIMAMURA, MASAYUKI HATTA, AKIRA NAGAFUCHI, AKINAO NOSE, MAYUMI MATSUNAGA, KOHEI HATTA, MASATOSHI TAKEICHI*

Cadherins are a family of Ca^{2+}-dependent intercellular adhesion molecules. Complementary DNAs encoding mouse neural cadherin (N-cadherin) were cloned, and the cell binding specificity of this molecule was examined. Mouse N-cadherin shows 92 percent similarity in amino acid sequence to the chicken homolog, while it shows 49 percent and 43 percent similarity to epithelial cadherin and to placental cadherin of the same species, respectively. In cell binding assays, mouse N-cadherin did not cross-react with other mouse cadherins, but it did cross-react with chicken N-cadherin. The results indicate that each cadherin type confers distinct adhesive specificities on different cells, and also that the specificity of N-cadherin is conserved between mammalian and avian cells.

THE ADHESIVE SELECTIVITY OF ANIMAL cells is thought to be crucial for controlling the association or movement of cells involved in embryonic morphogenesis (*1*). Cadherins are a family of intercellular adhesion receptors that may play a role in selective cell adhesion (*2*). Two members of this family, epithelial cadherin (E-cadherin), which is also called uvomorulin or cell CAM120/80 (*3, 4*), and placental cadherin (P-cadherin) (*5*), were characterized molecularly in the mouse. Two other members, liver cell adhesion molecule (L-CAM) (*6*) and neural cadherin (N-cadherin) (*7*), were identified in the chicken. The different cadherin types exhibit distinct tissue distribution patterns (*8*). Both E-cadherin and L-CAM are thought to be the interspecies homologs since they show a similar pattern of tissue distribution in the respective species (*8*).

Transferring cadherin cDNAs into heterologous cells allowed us to examine the role of cadherins in cell adhesion (*3, 7, 9*). We found that L cells transfected with E-cadherin cDNA sorted out from those transfected with P-cadherin cDNA when mixed (*10*), indicating that these cadherins have binding specificities. Moreover, when the E-cadherin–transfected L cells were added to a suspension of embryonic lung cells, they preferentially attached to the epithelial cells of this tissue, which also express E-cadherin (*10*). These results suggest that cadherins participate in cell sorting in embryonic tissues.

N-cadherin is expressed in various neural tissues (*11, 12*) and has been implicated in the attachment of axons to other cells (*13*), raising the possibility that this molecule is involved in neuronal recognition mechanism. To determine whether this cadherin

Department of Biophysics, Faculty of Science, Kyoto University, Kitashirakawa, Sakyo-ku, Kyoto 606, Japan.

*To whom correspondence should be addressed.